

# Theoretical Examination of Covalency in Berkelium(IV) Carbonate Complexes

Cristian Celis-Barros<sup>1</sup>, David Hobart<sup>1</sup>, Dayán Páez-Hernández<sup>2</sup>, and Thomas Albrech-Schmitt<sup>1</sup>

<sup>1</sup>Florida State University

<sup>2</sup>Universidad Andres Bello

May 5, 2020

## Abstract

Experimental studies on the speciation of berkelium in carbonate media have shown that complexation of berkelium(III) by carbonate results in spontaneous oxidation to berkelium(IV) and that multiple species can be present in solution. We studied two proposed structures present in solution based on theoretical comparisons with spectroscopic data previously reported for Bk(IV) carbonate solutions. The multiconfigurational character of the ground and low-lying excited states in both complexes is demonstrated to result from the strong spin-orbit coupling. Although bonding in berkelium(IV) carbonate and carbonate-hydroxide complexes is dominated by strong Coulombic forces, the presence of the non-negligible covalent character is supported by ligand-field theory, natural localized orbitals and topological studies of the electron density. Bond orders based in natural localized molecular orbitals (NLMOs) show that Bk–OH bonds possess enhanced orbital overlap that is reflected in the bond strength.

## Introduction

In the periodic table, berkelium is at a transition point between the lighter actinides exhibiting multiple oxidation states and the heavier actinides behaving more like the lanthanides that are dominated by the trivalent state.<sup>1</sup> Berkelium exhibits both the trivalent and tetravalent oxidation states that are stable in solution and solid state. Berkelium(IV) has special stability as a consequence of its half-filled shell  $5f^7$  electronic configuration. Because of the higher charge of tetravalent berkelium and its affinity for strong complexation by hard oxygen-donor ligands such as carbonate ions, Bk(IV) is more stable than Bk(III) in strongly complexing, concentrated, basic carbonate solutions. In fact, green Bk(III) auto-oxidizes in air in carbonate solutions to form yellow Bk(IV) complexes.<sup>2</sup>

There is an increased interest in berkelium chemistry because of its unique position in the periodic table, its importance as a target material for production of super-heavy elements, and the recent availability of multi-milligram quantities of the relatively long-lived isotope  $^{249}\text{Bk}$  ( $t_{1/2} = 330$  d).<sup>1,3</sup> In contrast, only a few reports of theoretical studies of Bk(III)<sup>4–6</sup> and Bk(IV)<sup>3,5,6</sup> complexes have been reported. Experimental, spectroscopic, and electrochemical studies of berkelium in concentrated basic aqueous carbonate solutions were published in the 1990's that demonstrated that carbonate ions stabilize Bk(IV).<sup>2,7</sup> The present study aims to give further theoretical insight into the electronic structure and bonding of Bk(IV) in carbonate and carbonate-hydroxide environments.

# Results and Discussion

## DFT Calculations

Since the geometry of berkelium carbonate complexes is unknown, we firstly modelled the initial structures. Hobart and coworkers<sup>2</sup> suggested two different structures according to their experimental studies varying the carbonate concentration and pH, one corresponding to the homoleptic carbonate complex and the second with coordination of hydroxyl ligands (carbonate-hydroxide). Fig. 1 shows the two structures obtained by DFT geometry optimizations with no symmetry constrains using a well-known eight-coordinated structure of berkelium(IV), multiple starting geometries were considered resulting always in structure **2**. These structures correspond to a  $C_{2V}$  and quasi- $C_{2V}$  symmetry for **1** and **2**, respectively (Table S1, ESI). Because previously published experimental absorption spectra of berkelium(IV) in carbonate solutions were available, Time-Dependent DFT (TD-DFT) calculations were carried out to understand the nature of the transitions responsible for the charge-transfer band with a peak at 273 nm (Fig. 2).

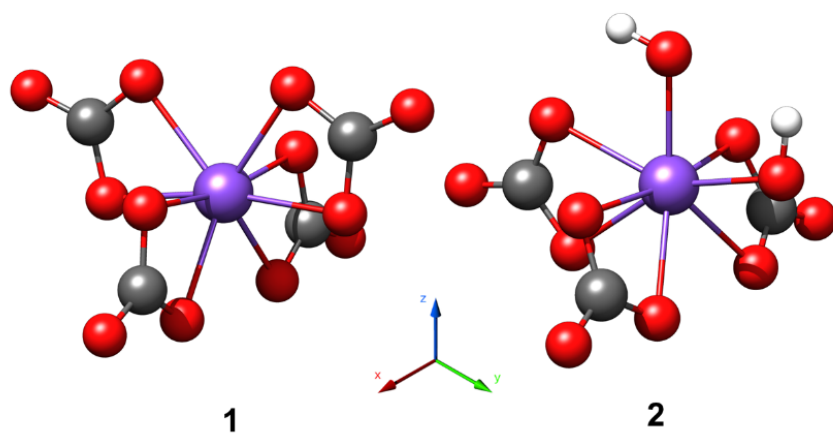


**Fig. 1.** Proposed optimized structures depicted with ball and sticks for  $[\text{Bk}(\text{CO}_3)_4]^{4+}$  (**1**) and  $[\text{Bk}(\text{CO}_3)_3(\text{OH})_2]^{4+}$  (**2**) complexes.

The calculated spectra seem to agree with the experimental data and the initial supposition of the replacement of one carbonate by two hydroxyl ligands that matches the experimental Bk(IV) spectrum in 2 M carbonate solution (Fig. 2). The peak corresponding to the pure carbonate coordinated structure was predicted to be located at 307.7 nm while the peak for the carbonate-hydroxide structure was predicted to be at 302.1 nm (Table 1). Unlike the homoleptic complex, an intense transition (370.9 nm) is observed in the calculated absorption spectrum of the heteroleptic complex that matches the shoulder observed in the 2 M carbonate spectrum.<sup>2</sup>

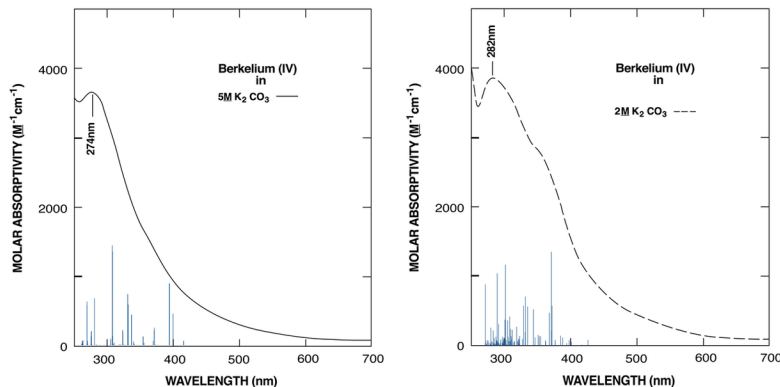


**Fig. 2.** Experimental UV-vis absorption spectra (redrawn from reference 2) of Bk(IV) in 5 M (left) and 2 M (left) potassium carbonate solutions. Blue lines represent transitions predicted by TD-DFT for  $[\text{Bk}(\text{CO}_3)_4]^{4-}$  (left) and  $[\text{Bk}(\text{CO}_3)_3(\text{OH})_2]^{4-}$  (right).

From the calculated spectra, it is possible to assign the band-decomposition of the spectra for both structures, wherein both cases are assigned to ligand-to-metal charge transfers (LMCT). However, the intense transition at 370.9 nm in the carbonate-hydroxide spectrum corresponds to a mixed molecular orbital involving sigma contribution coming from both carbonate and hydroxyl ligands.

**Table 1.** Selected TD-DFT transitions representing the LMCT band in the absorption spectra for **1** and **2**. The transitions presented are those with the highest oscillator strengths ( $f$ ).

$[\text{Bk}(\text{CO}_3)_4]^{4-}$	$[\text{Bk}(\text{CO}_3)_4]^{4-}$	$[\text{Bk}(\text{CO}_3)_3(\text{OH})_2]^{4-}$	$[\text{Bk}(\text{CO}_3)_3(\text{OH})_2]^{4-}$
$\lambda$ (nm)	$f$	$\lambda$ (nm)	$f$
280.2	$1.40 \cdot 10^{-2}$	289.6	$1.66 \cdot 10^{-2}$
307.7	$2.70 \cdot 10^{-2}$	302.1	$1.85 \cdot 10^{-2}$
331.1	$1.45 \cdot 10^{-2}$	332	$1.12 \cdot 10^{-2}$
394	$1.78 \cdot 10^{-2}$	370.9	$2.15 \cdot 10^{-2}$

This transition is also observed in the homoleptic structure (394.0 nm) where, due to the symmetry of the molecule, a lower change in the dipole moments is produced with respect to the carbonate-hydroxide complex. The substitution of one carbonate ligand by two hydroxyl ligands affects directly the transition dipole moment, resulting in an increase of the transition probability from 0.231 to 0.263 a.u. for the carbonate and carbonate-hydroxide complexes, respectively. This could explain the shoulder observed in the spectrum of the heteroleptic complex (Fig.2).

## Multiconfigurational calculations

The Bk(IV) free ion, considering a scalar relativistic limit and Hund's rule, has an  $^8\text{S}$  ground state ( $L=0$ ,  $S=7/2$ ) followed by a first excited multiplet  $^6\text{P} \sim 26500 \text{ cm}^{-1}$  higher in energy. The spin-orbit coupling (SOC) removes the state degeneracy resulting in a series of multiplets characterized by the total angular momentum quantum number ( $J$ ), with the ground term being (in a Russell-Saunders notation)  $^8\text{S}_{7/2}$ . If the ion is now placed in a ligand environment, the effect of the ligand field produces the split of the  $2J+1$  degenerate state and the mixing of states with different  $m_J$  values. This picture, based on a single ion structure, can be used in molecular systems where mixing between metal and ligand is negligible.

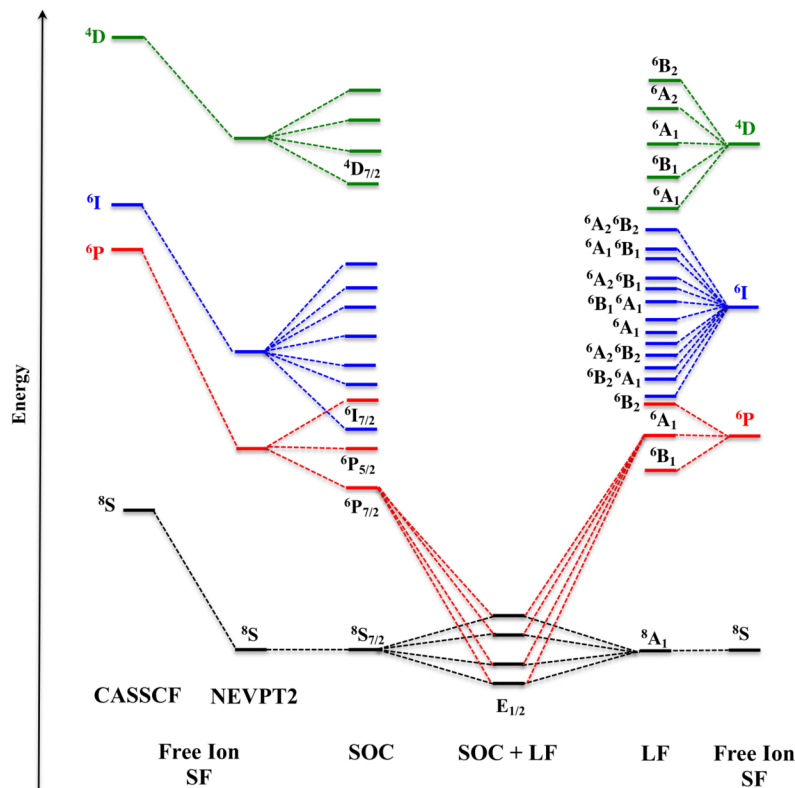


**Fig. 3.** Qualitative electronic states diagram considering ligand field (LF) effect after and before spin orbit coupling (SOC) in  $[\text{Bk}(\text{CO}_3)_4]^{4-}$ .

However, for molecules **1** and **2**, our calculations show significant mixing between symmetry adapted molecular orbitals of the ligands and the 5f shell, and therefore the electronic structure for both compounds should be discussed in terms of molecular states instead. If the ligand field effect is considered first, the 2L+1 degenerate free-ion states split the ground  $^8\text{A}_1$  that is then split again by spin orbit coupling giving rise to four  $\text{E}_{1/2}$  Kramer's doublets. These states, additionally, have contributions from the  $^6\text{A}_1$  and  $^4\text{A}_1$  states, which arise from the  $^6\text{P}$  and  $^4\text{D}$  atomic states, respectively. Fig. 3 shows a qualitative diagram of the electronic states in which both analyses explained above are summarized.

The calculations considering the minimal active space CAS(7,7) partially reproduce the nature of the molecular electronic states and are more similar to a single-ion behavior. We also performed full relativistic 4-component multiconfigurational calculations (GRASP2018)<sup>8</sup> on the Bk(IV) ion showing that the ground state of the unbound ion is composed by 85%  $^8\text{S}_{7/2}$  ( $^8\text{S}$ ) + 13%  $^6\text{P}_{7/2}$  ( $^6\text{P}$ ), and small contributions (less than 1%) from the  $^4\text{D}_{7/2}$ . A similar behavior is obtained by ligand-field DFT (LFDFT) (see Computational Details) with a wavefunction composed by 82%  $^8\text{S}_{7/2}$  + 16%  $^6\text{P}_{7/2}$  + 2%  $^4\text{D}_{7/2}$ . On the other hand, the ground state configuration of the free-ion was 90%  $^8\text{S}$  + 10%  $^6\text{P}$  at SOC-NEVPT2 with CAS(7,7) level of theory. The differences can be attributed to the limit of the NEVPT2 approach which can miss about 15-30% of the dynamical correlation effects<sup>9</sup> (Table S2, ESI). It is important to note that 4-component multiconfiguration calculations also lack dynamical correlation.

For complexes **1** and **2**, at the same level of theory, the ground state configuration was 87%  $^8\text{A}_1$  ( $^8\text{S}$ ) + 13%  $^6\text{A}_1$  ( $^6\text{P}$ ) (Table S3). The difference with respect to the free ion can be related with a direct effect of the ligand field, which stabilizes the first spin-free excited sextet by  $\sim 1900 \text{ cm}^{-1}$  increasing the contribution of  $^6\text{A}_1$  ( $^6\text{P}$ ) in the ground configuration. A significant reduction in the octuplet nature of the ground

state is seen within LFDFT, but similar in the stabilization of the sextet multiplet; with a composition of 69%  $^8A_1(^8S) + 23\% ^6A_1(^6P) + 4\% ^4A_1(^4D)$ . In parallel, it is helpful to establish differences between the lanthanide analog isoelectronic to Bk(IV), Gd(III). The calculations of  $[Gd(CO_3)_4]^{5-}$  reveal that the ground state  $^8S_{7/2}$  is almost degenerate ( $1.7 \text{ cm}^{-1}$ ) because the mixing of the excited states into the ground term is negligible (100%  $^8S_{7/2}$ ) (Table S2, ESI). On the other hand, Bk(IV) either as a free-ion or as a complex, shows a totally different picture because of the stronger spin-orbit coupling that mixes the  $^6P_{7/2}$  with the  $^8S_{7/2}$  in the ground state (Table 2, and Tables S2-S5 in ESI). Additionally, the ligand field interaction produces a significant change of the ground state of the actinide ion. Because of the electron correlation, CAS(13,10), the ground spin-free  $^8A_1$  state is stabilized, and the four  $E_{1/2}$  Kramer’s doublets experience a reduction in their energies. The configuration of the ground electronic state for **1** and **2** are 89%  $^8A_1(^8S) + 11\% ^6A_1(^6P)$  and 86%  $^8A_1(^8S) + 14\% ^6A_1(^6P)$ , respectively (Table 2).

**Table 2.** Energies ( $\text{cm}^{-1}$ ) and composition of the electronic ground multiplet  $J = 7/2$  relative to the ground state from a CAS(13,10) calculation. SO-CASSCF and SO-NEVPT2 differ in the dynamical energy correction by perturbation theory.

$[Bk(CO_3)_4]^{4-}$	$[Bk(CO_3)_4]^{4-}$	$[Bk(CO_3)_4]^{4-}$	$[Bk(CO_3)_4]^{4-}$
SO-CASSCF	SO-CASSCF	SO-NEVPT2	SO-NEVPT2
0	91% $^8A_1(^8S) + 9\% ^6A_1(^6P)$	0	89% $^8A_1(^8S) + 11\% ^6A_1(^6P)$
34.1	90% $^8A_1(^8S) + 10\% ^6A_1(^6P)$	44.6	90% $^8A_1(^8S) + 10\% ^6A_1(^6P)$
47.9	90% $^8A_1(^8S) + 10\% ^6A_1(^6P)$	64.3	89% $^8A_1(^8S) + 11\% ^6A_1(^6P)$
74.7	91% $^8A_1(^8S) + 9\% ^6A_1(^6P)$	94.5	88% $^8A_1(^8S) + 12\% ^6A_1(^6P)$
$[Bk(CO_3)_2(OH)_2]^{4-}$	$[Bk(CO_3)_2(OH)_2]^{4-}$	$[Bk(CO_3)_2(OH)_2]^{4-}$	$[Bk(CO_3)_2(OH)_2]^{4-}$
0	88% $^8A_1(^8S) + 12\% ^6A_1(^6P)$	0	86% $^8A_1(^8S) + 14\% ^6A_1(^6P)$
52.3	90% $^8A_1(^8S) + 10\% ^6A_1(^6P)$	74.7	87% $^8A_1(^8S) + 13\% ^6A_1(^6P)$
70.9	91% $^8A_1(^8S) + 9\% ^6A_1(^6P)$	96.8	88% $^8A_1(^8S) + 12\% ^6A_1(^6P)$
96.4	92% $^8A_1(^8S) + 8\% ^6A_1(^6P)$	141.1	89% $^8A_1(^8S) + 11\% ^6A_1(^6P)$

The role of the ligand field was also evaluated using the Condon-Slater parameters for interelectronic repulsion at CAS(7,7)SCF level though the so-called ab initio ligand field theory (AILFT). As was pointed out recently by Neese *et al.*, NEVPT2 results are not relevant to the bonding analysis and frequently introduce large errors.<sup>6</sup> As shown in Table 3 for both molecules, the ratio  $F^k/F^k_{\text{free-ion}} (k = 2, 4, 6) < 1$  with variations over 3%, which implies a nephelauxetic effect responsible for the reduction of the electron-electron repulsion due to the strong interaction of the 5f orbitals with the carbonate ligands. LFDFT yields similar parameters for the free-ion (Table 3), however they differ significantly when the molecular structure is considered, i.e.  $F^k$  and  $\zeta$  are reduced compared to AILFT; with reductions *ca.* 44% with respect to the free-ion. This shows a more effective penetration of the ligand’s electron cloud into that of the metal compared to AILFT<sup>6</sup>. The difference could reside in the localized description of f-electrons under HF and post-HF methods compared to the well-known overdelocalization of DFT; though, this could be argued against when using hybrid functionals as in this case. Carnall and coworkers have obtained these parameters from  $BkF_4$  experimental spectra.<sup>10,11</sup> These parameters are larger than those obtained by LFDFT, but in agreement with the nephelauxetic series. This could prove the effect of covalency on the reduction of the electrostatic repulsion in actinides.

The analysis of the optimized molecular orbitals shows an important bonding interaction between 5f and ligands orbitals. The active behavior of the ligand orbitals was corroborated through analysis of the occupation numbers after a careful inclusion of the symmetry adapted orbitals.

**Table 3.** One-electron Slater-Condon  $F^k$  ( $k = 2, 4, 6$ ) and effective spin-orbit coupling parameters

Parameter	CAS(7,7)	CAS(7,7)	CAS(7,7)	LFDFT	LFDFT	LFDFT
	$Bk^{4+}$ -free ion	$[Bk(CO_3)_4]^{4-}$	$[Bk(CO_3)_2(OH)_2]^{4-}$	$Bk^{4+}$ -free ion	$[Bk(CO_3)_4]^{4-}$	$[Bk(CO_3)_2(OH)_2]^{4-}$

Parameter	CAS(7,7)	CAS(7,7)	CAS(7,7)	LFDFFT	LFDFFT	LFDFFT
F <sup>2</sup>	91960	88983	88914	87058	48884	49288
F <sup>4</sup>	60505	58605	58725	57083	31818	32090
F <sup>6</sup>	44573	43295	43327	41991	23328	23530
$\zeta(5f)$	3589	3499	3499	3615	2607	2622

These orbitals were selected based on their bonding or antibonding character with respect to the 5f shell (Fig. 4). As shown, the occupation numbers show a dependence with the size of the active space. For both molecules, the minimal space given is  $f = 7$ , but when ligand orbitals are added to the 5f shell, occupation change to 7.32 and 7.59 for **1** and **2** respectively with CAS(13,10). This change implies the sharing of electrons between the ligand and the metal, allowing one to characterize the ligand-metal interaction partially covalent. It is important to note that the occupation numbers presented in Fig. 4 were obtained from an SCF calculation which, as known, has a localization error and therefore the prediction of the covalent character is underestimated. This means that other tools are necessary to obtain a better understanding of the nature of the bond and whether the electron density from the ligand is being localized into the metal or shared as an open-shell interaction.

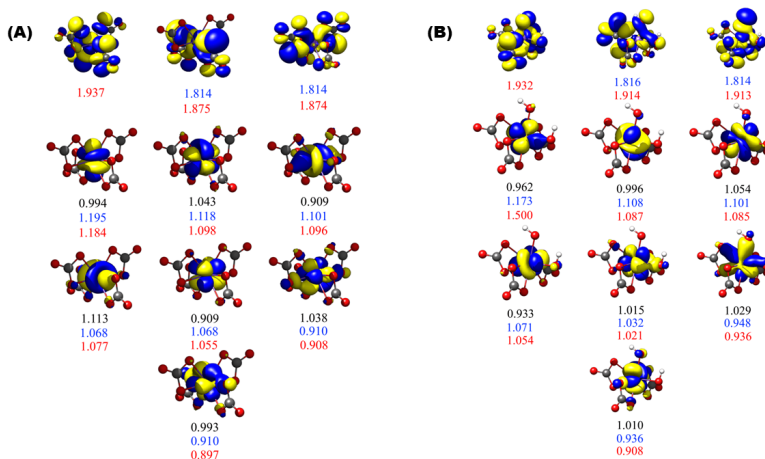


**Fig. 4.** Occupation numbers for the active orbitals in molecules (A) **1** and (B) **2**. Black, blue, and red numbers correspond to CAS(7,7), CAS(11,9), and CAS(13,10) active spaces.

## Natural Localized Molecular Orbitals (NLMOs)

Natural bond orbitals (NBO) is a well-known method to obtain the localized picture of the wavefunction. With the aid of NLMOs and bond orders the nature of the bond can be revealed. The Wiberg bond order, which does not recover differences between bonding and antibonding contributions in the natural atomic orbital (NAO) basis, is predicted to be 2.61 for both **1** and **2** complexes. The decomposition of this value into individual Bk–O contributions for each complex reveals that these two complexes are different (Table S5, ESI). Bk–OH bonds in complex **2** display the largest bond orders (*ca.*0.4), which implies that Bk–O<sub>CO3</sub> bond orders are decreased in this complex with respect to complex **1**.

Further insight into these differences can be obtained through analysis of localized molecular orbital (LMO) bond orders because they allow the decomposition of the bond order into NLMOs contributions. Table 4 (decomposition per bond in Table S6, ESI) summarizes LMO bond orders including the main contributor

to the bond order that corresponds to the  $\sigma$ -NLMO (Fig. 5). The overall values for Bk are 1.476 and 1.548 for **1** and **2**, respectively. Unlike Wiberg bond orders, these values differ from each other because LMO bond orders can discriminate between bonding and antibonding contributions, which make them more insightful into the strength of the bond. Nonetheless, the insight given by both is essentially the same, i.e. Bk–OH bonds display larger bond orders than Bk–O<sub>CO3</sub>. This picture agrees with the optimized bond distances (Table S1, ESI).

**Table 4.** Natural localized bond orders with the main  $\sigma$ -NLMOs contribution and their compositions.

	Bond*	Bond Order	NLMO	Composition
[Bk(CO <sub>3</sub> ) <sub>4</sub> ] <sup>4-</sup>	Bk–O(1)	0.19	0.72	7%Bk + 91%O + 1%C Bk (14% 7s + 51% 6d + 33% 5f)
	Bk–O(2)	0.17	0.71	7%Bk + 92%O + 1%C Bk (18% 7s + 59% 6d + 23% 5f)
Bk(CO <sub>3</sub> ) <sub>3</sub> (OH) <sub>2</sub> ] <sup>4-</sup>	Bk–O(1)	0.18	0.72	7%Bk + 92%O + 1%C Bk (17% 7s + 56% 6d + 27% 5f)
	Bk–O(2)	0.15	0.71	6%Bk + 92%O + 2%C Bk (16% 7s + 59% 6d + 25% 5f)
	Bk–OH(1)	0.27	0.72	8%Bk + 92%O Bk (18% 7s + 57% 6d + 25% 5f)
	Bk–OH(2)	0.25	0.71	8%Bk + 92%O Bk (17% 7s + 54% 6d + 28% 5f)

Looking at the contributions given in Table 4 and Table S6 in the ESI, it can be noted that in complex **1** the contribution to the bond order coming from  $\sigma$ -NLMOs ranges from 70-91% denoting a high predominance of the  $\sigma$ -character of the bond. On the other hand, for complex **2** a similar predominance for Bk–O<sub>CO3</sub> bonds is observed (74-87%) but significantly deviates for Bk–OH bonds (56%). This means that the bond order in the latter bonds is increased by  $\pi$  contributions.

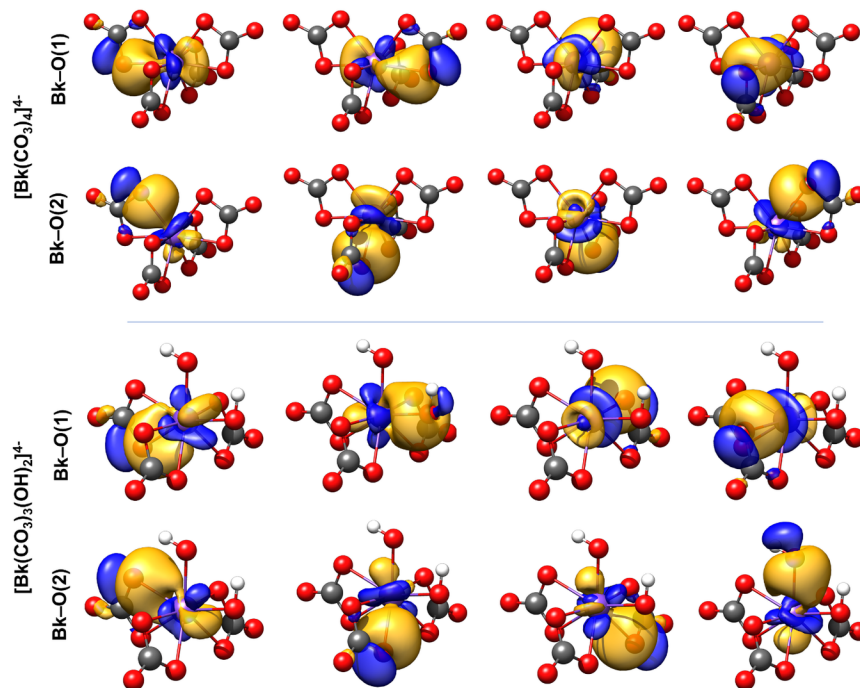


**Fig. 5.**  $\sigma$ -type NLMOs for complexes **1** and **2**. Second and fourth NLMOs in third and fourth rows correspond to Bk-OH(1) and Bk-OH(2), respectively.

## Topological analysis of the electron density

An alternative approach that provides further insight into the chemical bond is the Quantum Theory of Atoms in Molecules (QTAIM). Several theoretical studies on bonding in actinides have been reported, mainly by Kerridge,<sup>12–17</sup> while only a few experimental<sup>18–22</sup> studies have been reported. Studies devoted to the understanding of covalency in heavy actinides are scarce.<sup>19,21–23</sup> The virtue of QTAIM is that the partition of the 3D space is said to be natural since no chemical intuition is required.

Our results indicate that complexes **1** and **2** present differences in bonding based on their topology. The homoleptic carbonate complex shows higher concentrations of electron density at the BCP than Bk–O carbonate bonds in **2**. This occurs as a compensation of strengthened Bk–OH bonds creating the polarization of the delocalized electron density. From the energy density approach,<sup>24</sup> we observe in Table S7 (see ESI) that all bonds present a certain covalent character due to  $V(r)/G(r) > 1$  in all cases, implying negative values for the total energy density. The set of oxygen atoms lying in the  $xy$  plane (Table 5) present slightly larger  $H_{BCP}(r)$  values (*ca.*  $20 \text{ kJ mol}^{-1} \text{ \AA}^{-3}$ ) than Bk–O(2) in the complex **2**, whereas the opposite is true for complex **1** (*ca.*  $5 \text{ kJ mol}^{-1} \text{ \AA}^{-3}$  lower). On the other hand, Bk–OH bonds display significantly more negative total energy densities. Espinoza et al.<sup>25,26</sup> discussed total energy densities as the balance between pressure applied by electrons around the BCP (potential energy) and the reaction contrary to that pressure applied by the electrons at the BCP (kinetic energy). In this context, covalency is observed in all Bk(IV) bonds due to stronger pressure applied by the electrons around the BCP.

**Table 5.** QTAIM average metrics. Electron densities are given in  $e\text{\AA}^{-3}$ , energy densities in  $\text{kJ mol}^{-1}\text{\AA}^{-3}$ , and energies in  $\text{kJ mol}^{-1}$ . Extended table is found in ESI<sup>+</sup>.

	Bond*	$\rho_{\text{BCP}}(\mathbf{r})$	$\epsilon_{\text{BCP}}(\mathbf{r})$	$\delta_{\text{BCP}}(\mathbf{r})$	$H_{\text{BCP}}(\mathbf{r})$	$ H(\mathbf{r}) /\rho(\mathbf{r})$
	Bond*	$\rho_{\text{BCP}}(\mathbf{r})$	$\epsilon_{\text{BCP}}(\mathbf{r})$	$\delta_{\text{BCP}}(\mathbf{r})$	$H_{\text{BCP}}(\mathbf{r})$	$ H(\mathbf{r}) /\rho(\mathbf{r})$
[Bk(CO <sub>3</sub> ) <sub>4</sub> ] <sup>4-</sup>	Bk–O(1)	0.45	0.04	0.29	-143.9	323.3
	Bk–O(2)	0.45	0.03	0.29	-148.3	330.4
[Bk(CO <sub>3</sub> ) <sub>3</sub> (OH) <sub>2</sub> ] <sup>4-</sup>	Bk–O(1)	0.4	0.04	0.26	-100	246.6
	Bk–O(2)	0.38	0.02	0.24	-78.4	207.7
	Bk–OH(1)	0.56	0.13	0.39	-301.8	536.9
	Bk–OH(2)	0.57	0.09	0.4	-279	488.7

Furthermore, Espinosa et al.<sup>26</sup> introduced the concept of covalency degree as the total pressure per electron density unit around the BCP that is easily obtained by dividing  $H(\mathbf{r})$  by the electron density at that point. It represents a more balanced way to assess covalency in any pairwise interaction. Our results indicate essentially the same trend observed in total energy densities, though separations are more pronounced between Bk–O(1) Bk–O(2).

Further insight into the topology of these complexes can be obtained by looking at the localization ( $\lambda$ ) and delocalization ( $\delta$ ) indices (Table S7, ESI). These integrated parameters can be related to the bond orders and the actual oxidation state ( $Z - \lambda$ ) of Bk in the molecule. The calculated values assign the +4 oxidation state to both complexes that deviate significantly from calculations previously reported for Bk(IV) in a hexachloride environment (+3.345).<sup>5</sup> This could mirror the way that the ligands in complexes **1** and **2** coordinate to Bk(IV), where charge-transfer seems not to be as important as ionic and covalent interactions. The  $\delta_{\text{BCP}}$  parameters are similar in magnitude to the Wiberg bond orders (Table S5, ESI) reflecting the consistency of the results around the concept of bond order.

A final important remark regarding the electron density is the bond ellipticity. This parameter reveals the symmetry of the electron density along the bond-path. Thus, for pure  $\sigma$ -bonds a value of zero is expected to represent a cylindrically symmetric electron density; whereas, when  $\pi$  contributions take place in the bond, ellipticity deviates from zero. To put Bk–O bonds into perspective, a C–C bond in butane has an ellipticity of 0.01, while a C=C bond in ethene reaches a value of 0.3. As shown in Table 5, the ellipticity in Bk–CO<sub>3</sub> bonds is much more cylindrical than Bk–OH bonds, which confirms and agrees with the results shown in Table 4 based on the  $\sigma$  and  $\pi$  contributions to the bond order.

## Interacting Quantum Atom (IQA)

As a final approach to shed lights on covalency, IQA<sup>27</sup> provides a way to measure covalency in terms of energy decomposition by separating contributions from purely Coulomb/electrostatic and exchange (exchange-correlation in case of DFT) interactions between two topological atoms (basins). It is noteworthy that these energies are evaluated by integrating over the basins and have no direct relation to properties obtained at the BCP. Table 6 (decomposition per bond in Table S8, ESI) shows this decomposition analysis for complexes **1** and **2**. The behavior of energy densities in Table 5 can be understood by the role of exchange interactions in the total energy of interaction between Bk and O basins. Thus, within IQA, covalency is seen as the weight that exchange energies have in the overall energy of interaction. The results indicate that complex **1** has the same covalent character in the Bk–O(1) and Bk–O(2) bonds. Thus, the small difference observed for the total energy of interaction  $E_{\text{INT}}$  in **1** is due to Coulombic interactions, though this difference is negligible. In contrast, a total rearrangement is observed in complex **2**. Exchange interactions are decreased in Bk–O bonds due to the strengthening of the Bk–OH bonds and particularly the Bk–OH(1) bond with the concomitant weakening of the opposed berkelium carbonate bonds. This is reflected in the nearly 3% increase of covalency in the bonds.

**Table 6.** IQA energy decomposition.  $E_C$  corresponds to Coulombic energies,  $E_X$  to exchange energies, and  $E_{INT}$  refers to total energy of interaction ( $E_C + E_X$ ) between Bk and O atoms. Covalent energy is expressed as the weight that exchange interactions have in the total energy. Average energies are given in  $\text{kJ mol}^{-1}$ . Detailed table is found in ESI

Bond*	$E_C$	$E_X$	$E_{INT}$	Exchange(%)
Bk-O(1)	-2364.1	-166	-2530	6.6
Bk-O(2)	-2365	-166	-2531.1	6.6
Bk-O(1)	-2417.6	-143.8	-2561.4	5.6
Bk-O(2)	-2411	-141.6	-2552.6	5.6
Bk-OH(1)	-2490.5	-238.7	-2729.2	8.7
Bk-OH(2)	-2412	-229.8	-2641.9	8.7

Although, complexes **1** and **2** display differences in the nature of the bonds, the overall bonding properties of Bk(IV) are quite the same (Table S8, ESI). This means that the ‘availability’ of Bk(IV) to form Bk–O bonds is essentially the same, but the way it forms those bonds is tunable. It would be interesting to see if this holds for Bk(IV) bonds other than oxygen-donor ligands.

## Conclusions

Through this study, we have shown some aspects of the chemistry of Bk(IV) carbonate and carbonate-hydroxide complexes based on experimental studies reported three decades ago. The covalent character of the bonds has been deconvoluted by different approaches utilizing correlated wavefunctions showing variations in the bond due to increased orbital overlap as in the case of Bk–OH bonds. This implies stronger coordination of hydroxyl ions over the carbonate ions, which could be related to the displacement of carbonate ions from the first sphere of coordination of Bk(IV) in basic solutions. The role of the symmetry in the strength of the bond has also been exposed by the weakening of the bond of the carbonate opposite to OH(1).

The importance of integrating multiple theoretical approaches, even those seemingly opposed in nature, as the non-overlapping picture of the atoms in molecules with the overlap-based theory of NBO, is crucial in obtaining a full picture of these elusive actinide systems. Furthermore, using the concept of overlapping atoms, the increased orbital overlap in Bk–OH bonds leaves the question open as to if covalency in heavy elements is driven solely by energy orbital matching.<sup>19,28</sup>

## Computational Details

In this study, two models have been used to understand the arrangement of the environment of Bk(IV) in carbonate and carbonate-hydroxide solutions. All calculations herein, except ligand-field DFT (LFDFT), were performed using the ORCA 4.1 package.<sup>29</sup> For DFT optimizations of the molecular structures, we utilized the scalar relativistic all-electron Douglas-Kroll-Hess Hamiltonian (DKH), the PBE0 hybrid functional, and a SARC-DKH-TZVP basis set for the Bk(IV) atom and def2-TZVP for all the other atoms. No symmetry constraints were used. TD-DFT was used to model the UV-vis spectrum of the two optimized models. Kohn-Sham density functional theory with approximate functionals has proven to be remarkably successful given its relative simplicity and efficiency. However, it is well known that DFT produces an important delocalization error responsible for overestimation of covalency, which has an impact in the correct prediction of the ground state and spectroscopic properties. These problems can be solved in part using detailed parameterizations principally in the interelectronic terms. A good example of these functionals is the Coulomb attenuating method, CAM-B3LYP functional,<sup>30</sup> which was developed to minimize deviations

in charge-transfer excitation energies and used in this work to reproduce the absorption spectra of both carbonate compounds. It is important to note the recent study of Yang et al.<sup>31</sup>, which is the closer DFT study to heavy actinides using this class of functionals. In this context, this work represents one of the first studies where the performance of CAM-B3LYP functional is applied to heavy actinides.

The Complete Active Space Self-Consistent Field (CASSCF) approach combined with NEVPT2 for the inclusion of both, static and dynamic correlation, allows the construction of the configuration of all possible multiplicities within a determined active orbital space. Additionally, state mixing due to spin-orbit (SO) coupling can be accounted for via quasi-degenerate perturbation theory approach (QDPT). The effect of the dynamic correlation is included in the QDPT step as a diagonal correction of the nonrelativistic state energies. This combination of tools has been shown to be an effective methodology in the description of actinide compounds. The CASSCF/NEVPT2 approach provides a reliable treatment of the multiconfigurational character present in open-shell actinide systems and can be used with all-electron relativistic Hamiltonians. The CASSCF calculations were carried out using, initially, a minimal active space, which corresponds to the seven 5f electrons of the Bk(IV) ion in seven 5f orbitals. This active space was then augmented to a CAS(11,9) and finally to a CAS(13,10), including two and three symmetry adapted ligand orbitals respectively, which were selected based on its Bk–O bonding or antibonding character and 5f contribution. The 6d shell of orbitals was also considered. However, the occupation numbers of these orbitals were less than 0.02, so they were omitted in the results and discussion section.

Ligand-field theory was also considered for this study from two perspectives, *ab initio* (AILFT) and DFT (LFDFT)<sup>32</sup>. The former was calculated from the CASSCF matrix within ORCA, whereas the latter was performed in ADF2019<sup>33,34</sup>. LFDFT was performed based on Kohn-Sham orbitals calculated at ZORA/PBE0/TZP level of theory.

To obtain a better understanding of the nature of the chemical bond, Natural Bond Orbital (NBO) analyses were performed on correlated wavefunctions to localize orbitals. The NBO analysis is helpful to understand the Lewis picture of bonding by performing a transformation of the wavefunction into a localized form. NBOs are conceived as a set of localized bonds and lone pairs as basic units, where delocalization effects are missing from the molecular orbital (MO) perspective. However, there is an intermediate approach that recovers the MO perspective in the natural localized framework called the natural localized molecular orbitals (NLMOs).<sup>35</sup> These calculations were carried out using the Weinhold’s package NBO6<sup>36</sup> attached to ORCA.

Another tool especially developed to gain a deeper comprehension on the nature of bonding in molecular systems is the Bader’s quantum theory of atoms in molecules (QTAIM).<sup>37</sup> QTAIM parameters at the bond critical points (BCPs) such as the electron density  $\rho_{\text{BCP}}(\mathbf{r})$ , Laplacian of the electron density  $[\Delta]\rho_{\text{BCP}}(\mathbf{r})$ , delocalization  $\delta_{\text{BCP}}(\mathbf{r})$  and localization  $l$  indices, and total energy densities  $H_{\text{BCP}}(\mathbf{r})$  are commonly used to characterize the nature of bonds. It is well-known that covalent bonds or open-shell interactions, in terms of QTAIM metrics, present  $\rho_{\text{BCP}}(\mathbf{r}) > 0.2$  a.u. with  $[\Delta]\rho_{\text{BCP}}(\mathbf{r}) < 0$  and  $H_{\text{BCP}}(\mathbf{r}) < 0$ , while  $\rho_{\text{BCP}}(\mathbf{r}) < 0.1$  a.u. with  $[\Delta]\rho_{\text{BCP}}(\mathbf{r}) > 0$  and  $H_{\text{BCP}}(\mathbf{r}) > 0$  represent ionic, van der Waals or hydrogen bonds (closed-shell interactions). However, as Kerridge pointed out, there is no *a priori* reason to assume this convention for f-element chemistry.<sup>13</sup> On the other hand, delocalization and localization indices are useful to quantify the bond order and calculate the partial oxidation states, respectively.<sup>38</sup>

Additionally, the Interacting Quantum Atom (IQA)<sup>27</sup> energy partition analysis have been carried out. This complementary tool to understand the chemical bond under the framework of nonoverlapping quantum atoms decomposes the total energy of interaction between two topological atoms into Coulomb and exchange-correlation contributions. These calculations are obtained by 6-dimensional integration over the whole electron density between the two topological atoms, which uses the 2-electron density matrix (2EDM).

QTAIM parameters and IQA energies were calculated using the AIMAll software developed by Todd Keith.<sup>39</sup> All parameters reported herein were based on multiconfigurational wavefunctions. For post-HF wavefunctions, AIMAll uses the Muller approximation<sup>40</sup> to obtain the 2EDM due to the high computational costs involved in obtaining the exact matrix.

## Acknowledgements

This material is based upon work supported by the U.S. Department of Energy, Office of Science, Office of Basic Energy Sciences, Heavy Elements Chemistry Program under Award Number DE-FG02-13ER16414. The authors also acknowledge support by the Government of Chile, SA through Fondecyt No. 1180017.

## Conflict of interest

There are no conflicts to declare.

## ORCID

Cristian Celis-Barros 0000-0002-4685-5229

Dayán Páez-Hernández 0000-0002-8163-1343

Thomas Albrecht-Schmitt 0000-0002-2989-3311

## References

1. L. Morss, N. Edelstein and J. Fuger, *The Chemistry of the Actinide and Transactinide Elements*, Springer Netherlands, Dordrecht, **2011**.
2. D. E. Hobart, D. E. Morris, P. D. Palmer, R. G. Haire and J. R. Peterson, *Radiochim. Acta*, **1990**, 49, 119–124.
3. G. J.-P. Deblonde, M. Sturzbecher-Hoehne, P. B. Rupert, D. D. An, M.-C. Illy, C. Y. Ralston, J. Brabec, W. A. de Jong, R. K. Strong and R. J. Abergel, *Nat. Chem.*, **2017**, 9, 843–849.
4. A. Kovács, R. J. M. Konings, J. K. Gibson, I. Infante and L. Gagliardi, *Chem. Rev.*, **2015**, 115, 1725–1759.
5. C. Celis-Barros, D. Páez-Hernández, M. J. Beltrán-Leiva and R. Arratia-Perez, *Phys. Chem. Chem. Phys.*, **2018**, 20.
6. J. Jung, M. Atanasov and F. Neese, *Inorg. Chem.*, **2017**, 56, 8802–8816.
7. D. E. Morris, D. E. Hobart, P. D. Palmer, R. G. Haire and J. R. Peterson, *Radiochim. Acta*, **1990**, 49, 125–134.
8. C. Froese Fischer, G. Gaigalas, P. Jönsson and J. Bieroń, *Comput. Phys. Commun.*, **2019**, 237, 184–187.
9. M. Spivak, C. Angeli, C. J. Calzado and C. de Graaf, *J. Comput. Chem.*, **2014**, 35, 1665–1671.
10. W. T. Carnall and H. M. Crosswhite, in *The Chemistry of the Actinide Elements*, Springer Netherlands, Dordrecht, **1986**, pp. 1235–1277.
11. G. K. Liu, W. T. Carnall, G. Jursich and C. W. Williams, *J. Chem. Phys.*, **1994**, 101, 8277–8289.
12. P. Di Pietro and A. Kerridge, *Inorg. Chem.*, **2016**, 55, 573–583.
13. A. Kerridge, *Chem. Commun.*, **2017**, 53, 6685–6695.
14. A. Kerridge, *RSC Adv.*, **2014**, 4, 12078–12086.
15. A. Kerridge, *Dalt. Trans.*, **2013**, 42, 16428.

16. A. Formanuik, A.-M. Ariciu, F. Ortu, R. Beekmeyer, A. Kerridge, F. Tuna, E. J. L. McInnes and D. P. Mills, *Nat. Chem.* ,**2016** , 9, 578–583.
17. I. Fryer-Kanssen, J. Austin and A. Kerridge, *Inorg. Chem.* ,**2016** , 55, 10034–10042.
18. S. G. Minasian, J. L. Krinsky and J. Arnold, *Chem. - A Eur. J.* , **2011** , 17, 12234–12245.
19. M. P. Kelley, J. Su, M. Urban, M. Luckey, E. R. Batista, P. Yang and J. C. Shafer, *J. Am. Chem. Soc.* , **2017** , 139, 9901–9908.
20. A. J. Gaunt, S. D. Reilly, A. E. Enriquez, B. L. Scott, J. A. Ibers, P. Sekar, K. I. M. Ingram, N. Kaltsoyannis and M. P. Neu, *Inorg. Chem.* , **2008** , 47, 29–41.
21. M. A. Silver, S. K. Cary, A. J. Garza, R. E. Baumbach, A. A. Arico, G. A. Galmin, K.-W. Chen, J. A. Johnson, J. C. Wang, R. J. Clark, A. Chemey, T. M. Eaton, M. L. Marsh, K. Seidler, S. S. Galley, L. Van De Burgt, A. L. Gray, D. E. Hobart, K. Hanson, S. M. Van Cleve, F. Gendron, J. Autschbach, G. E. Scuseria, L. Maron, M. Speldrich, P. Kögerler, C. Celis-Barros, D. Páez-Hernández, R. Arratia-Pérez, M. Ruf and T. E. Albrecht-Schmitt, *J. Am. Chem. Soc.* , **2017** , 139.
22. M. J. Polinski, E. B. Garner, R. Maurice, N. Planas, J. T. Stritzinger, T. G. Parker, J. N. Cross, T. D. Green, E. V. Alekseev, S. M. Van Cleve, W. Depmeier, L. Gagliardi, M. Shatruk, K. L. Knappenberger, G. Liu, S. Skanthakumar, L. Soderholm, D. a Dixon and T. E. Albrecht-Schmitt, *Nat. Chem.* , **2014** , 6, 387.
23. A. Chandrasekar and T. K. Ghanty, *Inorg. Chem.* ,**2019** , 58, 3744–3753.
24. D. Cremer and E. Kraka, *Angew. Chemie Int. Ed. English* ,**1984** , 23, 627–628.
25. E. Espinosa, E. Molins and C. Lecomte, *Chem. Phys. Lett.* ,**1998** , 285, 170–173.
26. E. Espinosa, I. Alkorta, J. Elguero and E. Molins, *J. Chem. Phys.* , **2002** , 117, 5529–5542.
27. M. A. Blanco, A. Martín Pendás and E. Francisco, *J. Chem. Theory Comput.* , **2005** , 1, 1096–1109.
28. J. N. Cross, J. Su, E. R. Batista, S. K. Cary, W. J. Evans, S. A. Kozimor, V. Mocko, B. L. Scott, B. W. Stein, C. J. Windorff and P. Yang, *J. Am. Chem. Soc.* , **2017** , 139, 8667–8677.
29. F. Neese, *Wiley Interdiscip. Rev. Comput. Mol. Sci.* ,**2018** , 8, e1327.
30. T. Yanai, D. P. Tew and N. C. Handy, *Chem. Phys. Lett.* ,**2004** , 393, 51–57.
31. T. J. Duignan, J. Autschbach, E. Batista and P. Yang, *J. Chem. Theory Comput.* , **2017** , 13, 3614–3625.
32. H. Ramanantoanina, W. Urland, F. Cimpoesu and C. Daul, *Phys. Chem. Chem. Phys.* , **2013** , 15, 13902–13910.
33. G. te Velde, F. M. Bickelhaupt, E. J. Baerends, C. Fonseca Guerra, S. J. A. van Gisbergen, J. G. Snijders and T. Ziegler, *J. Comput. Chem.* , **2001** , 22, 931–967.
34. ADF 2019.3, SCM, **2019** , Theoretical Chemistry, Vrije Universiteit, Amsterdam, The Netherlands. <http://www.scm.com>.
35. A. E. Reed and F. Weinhold, *J. Chem. Phys.* , **1985** , 83, 1736–1740.
36. NBO6. E. D. Glendening, J. K. Badenhoop, A. E. Reed, J. E. Carpenter, J. A. Bohmann, C. M. Morales, C. R. Landis and F. Weinhold,**2013** .
37. R. Bader, *Atoms in Molecules* , Oxford University Press, Oxford, **1990** .
38. P. L. A. Popelier, in *The Chemical Bond II* , SpringerLink,**2016** , pp. 71–117.
39. AIMAll (version 17.01.25). T. A. Keith, **2017** , TK Gristmill Software, Overland Park KS.
40. A. M. K. Müller, *Phys. Lett. A* , **1984** , 105, 446–452.